ARMY RESEARCH LABORATORY

Generating an Aerodynamic Model for Projectile Flight Simulation Using Unsteady, Time Accurate Computational Fluid Dynamic Results

by Joseph Kokes, Mark Costello, and Jubaraj Sahu

ARL-CR-577 **September 2006**

prepared by

Oregon State University
Corvallis, OR 97331

Georgia Institute of Technology
Atlanta, GA 30332

U.S. Army Research Laboratory
Aberdeen Proving Ground, MD 21005

under contract

W911QX-05-P-0558 P00002

NOTICES

Disclaimers

The findings in this report are not to be construed as an official Department of the Army position unless so designated by other authorized documents.

Citation of manufacturer's or trade names does not constitute an official endorsement or approval of the use thereof.

Destroy this report when it is no longer needed. Do not return it to the originator.

Army Research Laboratory
Aberdeen Proving Ground, MD 21005-5066

ARL-CR-577 **September 2006**

Generating an Aerodynamic Model for Projectile Flight Simulation Using Unsteady, Time Accurate Computational Fluid Dynamic Results

Joseph Kokes
Oregon State University

Mark Costello
Georgia Institute of Technology

Jubaraj Sahu
Weapons and Materials Research Directorate, ARL

prepared by

Oregon State University
Corvallis, OR 97331

Georgia Institute of Technology
Atlanta, GA 30332

U.S. Army Research Laboratory
Aberdeen Proving Ground, MD 21005

under contract

W911QX-05-P-0558 P00002

REPORT DOCUMENTATION PAGE

Form Approved
OMB No. 0704-0188

1. REPORT DATE *(DD-MM-YYYY)*	2. REPORT TYPE	3. DATES COVERED (From - To)
September 2006	Final	November 2005–August 2006

4. TITLE AND SUBTITLE
Generating an Aerodynamic Model for Projectile Flight Simulation Using Unsteady, Time Accurate Computational Fluid Dynamic Results

5a. CONTRACT NUMBER
W911QX-05-P-0558 P00002

5b. GRANT NUMBER

5c. PROGRAM ELEMENT NUMBER

6. AUTHOR(S)
Joseph Kokes,[*] Mark Costello,[†] and Jubaraj Sahu

5d. PROJECT NUMBER
622618.H80

5e. TASK NUMBER

5f. WORK UNIT NUMBER

7. PERFORMING ORGANIZATION NAME(S) AND ADDRESS(ES)
Oregon State University, Corvallis, OR 97331
Georgia Institute of Technology, Atlanta, GA 30332
U.S. Army Research Laboratory, Aberdeen Proving Ground, MD 21005

8. PERFORMING ORGANIZATION REPORT NUMBER

9. SPONSORING/MONITORING AGENCY NAME(S) AND ADDRESS(ES)
U.S. Army Research Laboratory
ATTN: AMSRD-ARL-WM-BC
Aberdeen Proving Ground, MD 21005-5066

10. SPONSOR/MONITOR'S ACRONYM(S)
ARL-CR-577

11. SPONSOR/MONITOR'S REPORT NUMBER(S)

12. DISTRIBUTION/AVAILABILITY STATEMENT
Approved for public release; distribution is unlimited.

13. SUPPLEMENTARY NOTES
[*]Oregon State University, Corvallis, OR 97331
[†]Georgia Institute of Technology, Atlanta, GA 30332

14. ABSTRACT

A method to efficiently generate a complete aerodynamic description for projectile flight dynamic modeling is described. At the core of the method is an unsteady, time accurate computational fluid dynamics simulation that is tightly coupled to a rigid body dynamics simulation. A set of *n* short time snippets of simulated projectile motion at *m* different Mach numbers is computed and employed as baseline data. For each time snippet, aerodynamic forces and moments and the full rigid body state vector of the projectile are known. With time synchronized air loads and state vector information, aerodynamic coefficients can be estimated with a simple fitting procedure. By inspecting the condition number of the fitting matrix, it is straightforward to assess the suitability of the time history data to predict a selected set of aerodynamic coefficients. To highlight the merits of this technique, it is exercised on example data for a fin-stabilized projectile. The technique is further exercised for a fin- and spin-stabilized projectile using simulated data from a standard trajectory code.

15. SUBJECT TERMS
aerodynamic coefficients, trajectory, unsteady CFD, flight dynamics

16. SECURITY CLASSIFICATION OF:			17. LIMITATION OF ABSTRACT	18. NUMBER OF PAGES	19a. NAME OF RESPONSIBLE PERSON
a. REPORT	b. ABSTRACT	c. THIS PAGE			Jubaraj Sahu
UNCLASSIFIED	UNCLASSIFIED	UNCLASSIFIED	UL	34	19b. TELEPHONE NUMBER (*Include area code*) 410-278-3707

Standard Form 298 (Rev. 8/98)
Prescribed by ANSI Std. Z39.18

Contents

List of Figures

1. Introduction

There are roughly four classes of techniques to predict aerodynamic forces and moments on a projectile in atmospheric flight: empirical methods, wind tunnel testing, computational fluid dynamics simulation, and spark range testing. Empirical techniques aerodynamically describe the projectile with a set of geometric properties (diameter, number of fins, nose type, nose radius, etc.) and catalog aerodynamic coefficients of many different projectiles as a function of these features. The database of aerodynamic coefficients as a function of projectile features is typically obtained from wind tunnel or spark range tests. This data is fit to multivariable equations to create generic models for aerodynamic coefficients as a function of these basic projectile geometric properties. Examples of this approach to projectile aerodynamic coefficient estimation include Missile DATCOM, PRODAS, and AP98 (*1–6*). The advantage of this technique is that it is a general method applicable to any projectile. However, it is the least accurate method of the four methods just mentioned, particularly for new configurations that fall outside the realm of projectiles used to form the basic aerodynamic database. The empirical method has been found very useful in conceptual design of projectiles where rapid and inexpensive estimates of aerodynamic coefficients are needed.

In wind tunnel testing, a specific projectile is mounted in a wind tunnel at various angles of attack with aerodynamic forces and moments measured at various Mach numbers using a sting balance. Wind tunnel testing has the obvious advantage of being based on direct measurement of aerodynamic forces and moments on the projectile. It is also relatively easy to change the wind tunnel model to allow detailed parametric effects to be investigated. The main disadvantage to wind tunnel testing is that it requires a wind tunnel, which is modestly expensive. Furthermore, dynamic derivatives, such as pitch and roll damping, as well as, Magnus force and moment coefficients, are difficult to obtain in a wind tunnel and require a complex physical wind tunnel model. Wind tunnel testing is often used during projectile development programs to converge on fine details of the aerodynamic design of the shell (*7*, *8*).

In computational fluid dynamics (CFD) simulation, the fundamental fluid dynamic equations are numerically solved for a specific configuration. The most sophisticated computer codes are capable of unsteady time accurate computations using the Navier-Stokes equations. Examples of these tools include, for example, CFD++, Fluent, and Overflow-D. Over the past couple of decades, tremendous strides have been made in the application of CFD for prediction of aerodynamic loads on air vehicles, including projectiles. This numerical technique is based on first principles and does not involve physical testing. It is a general method that is valid for any projectile configuration. However, CFD is computationally expensive and requires powerful computers to obtain results in a reasonably timely manner (*9–22*). In spark range aerodynamic

testing, a projectile is fired through an enclosed building. At a discrete number of points during the flight of the projectile (<30) the state of the projectile is measured using spark shadowgraphs (*23–27*). The projectile state data is subsequently fit to a rigid 6 degree-of-freedom projectile model using the aerodynamic coefficients as the fitting parameters (*28–30*). Spark range aerodynamic testing is considered the gold standard for projectile aerodynamic coefficient estimation. It is the most accurate method for obtaining aerodynamic data on a specific projectile configuration. It is usually the most expensive alternative, requires a spark range facility, and is only valid for the specific projectile configuration tested.

Various researchers have used CFD to estimate aerodynamic coefficient estimation of projectiles. Early work focused on Euler solvers applied to steady flow problems, while more recent work has solved the Reynolds averaged Navier-Stokes equations and large eddy simulation Navier-Stokes equations for both steady and unsteady conditions (*9–22*). For example, to predict pitch damping, Weinacht prescribed projectile motion to mimic a typical pitch damping wind tunnel test in a CFD simulation to estimate the different components of the pitch damping coefficient of a fin-stabilized projectile (*31*). Excellent agreement between computed and measured pitch damping was attained. Algorithm and computing advances have also led to coupling of CFD codes to projectile rigid body dynamics codes for simulation of free flight motion of a projectile in a time-accurate manner. Aerodynamic forces and moments are computed with the computational fluid dynamics solver, while the free flight motion of the projectile is computed by integrating the rigid body dynamic (RBD) equations of motion. The ability to simulate the flight of a projectile using first principles has led to the notion of "virtual fly outs" where the simulation tools are used to replicate a spark range test. Along these lines, Sahu achieved excellent agreement between spark range measurements and a coupled CFD/RBD approach for a finned stabilized projectile (*32*). Projectile position and orientation at down-range locations consistent with a spark range test were extracted from the output of the CFD/RBD software to compute aerodynamic coefficients. Standard range reduction software was utilized for this purpose where good agreement was obtained in comparison to example spark range results.

While coupled CFD/RBD simulation is now capable of replicating time accurate projectile motion, computing time for this type of analysis is exceedingly high and does not currently represent a practical method for typical flight dynamic analysis, such as impact point statistics (circular error probable) computation where thousands of fly-outs are required. Furthermore, this type of analysis does not allow the same level of understanding of the inherent underlying dynamics of the system that rigid body dynamic analysis using aerodynamic coefficients yields. However, the coupled CFD/RBD approach does offer an ideal way to rapidly compute the aerodynamic coefficients needed for rigid 6 degree-of-freedom simulation. During a time-accurate CFD/RBD simulation, aerodynamic forces and moments, and the full rigid body state vector of the projectile are generated at each time step in the simulation. This means that aerodynamic forces, aerodynamic moments, position of the mass center, body orientation, translational velocity, and angular velocity of the projectile are all known at the same time

instant. With time-synchronized air load and state vector information, the aerodynamic coefficients can be estimated with a simple fitting procedure. This report creates a method to efficiently generate a complete aerodynamic model for a projectile in atmospheric flight using n short time histories at m different Mach numbers with an industry standard time-accurate CFD/RBD simulation. The technique is exercised on example CFD/RBD data for a small fin-stabilized projectile. The technique is further exercised for a fin- and spin-stabilized projectile using simulated data from a standard trajectory code. Parametric trade studies investigating the number of time snippets and the length of each time snippet to obtain accurate aerodynamic coefficients are reported.

2. Projectile CFD/RBD Simulation

The projectile CFD/RBD algorithm employed here combines a rigid 6 degree-of-freedom projectile flight dynamic model with a three-dimensional (3-D), time-accurate CFD simulation. The RBD dynamic equations are integrated forward in time, where aerodynamic forces and moments that drive motion of the projectile are computed using the CFD algorithm.

The RBD projectile model allows for 3 translation degrees of freedom and 3 rotation degrees of freedom. As shown in figures 1 and 2, the I frame is attached to the ground while the B frame is fixed to the projectile, with the $\vec{I}_B$ axis pointing out the nose of the projectile and the $\vec{J}_B$ and $\vec{K}_B$ unit vectors forming a right-handed triad. The projectile state vector is comprised of the inertial position components of the projectile mass center (x, y, z), the standard aerospace sequence Euler angles (ϕ, θ, ψ), the body frame components of the projectile mass center velocity (u, v, w), and the body frame components of the projectile angular velocity vector (p, q, r). Both the translational and rotational dynamic equations are expressed in the projectile body reference frame. The standard rigid projectile and body frame equations of motion are given by equations 1–4.

$$\begin{Bmatrix} \dot{x} \\ \dot{y} \\ \dot{z} \end{Bmatrix} = \begin{bmatrix} c_\theta c_\psi & s_\phi s_\theta c_\psi - c_\phi s_\psi & c_\phi s_\theta c_\psi + s_\phi s_\psi \\ c_\theta s_\psi & s_\phi s_\theta s_\psi + c_\phi c_\psi & c_\phi s_\theta s_\psi - s_\phi c_\psi \\ -s_\theta & s_\phi c_\theta & c_\phi c_\theta \end{bmatrix} \begin{Bmatrix} u \\ v \\ w \end{Bmatrix}. \tag{1}$$

$$\begin{Bmatrix} \dot{\phi} \\ \dot{\theta} \\ \dot{\psi} \end{Bmatrix} = \begin{bmatrix} 1 & s_\phi t_\theta & c_\phi t_\theta \\ 0 & c_\phi & -s_\phi \\ 0 & s_\phi / c_\theta & c_\phi / c_\theta \end{bmatrix} \begin{Bmatrix} p \\ q \\ r \end{Bmatrix}. \tag{2}$$

$$\begin{Bmatrix} \dot{u} \\ \dot{v} \\ \dot{w} \end{Bmatrix} = \begin{Bmatrix} X/m \\ Y/m \\ Z/m \end{Bmatrix} - \begin{bmatrix} 0 & -r & q \\ r & 0 & -p \\ -q & p & 0 \end{bmatrix} \begin{Bmatrix} u \\ v \\ w \end{Bmatrix}. \tag{3}$$

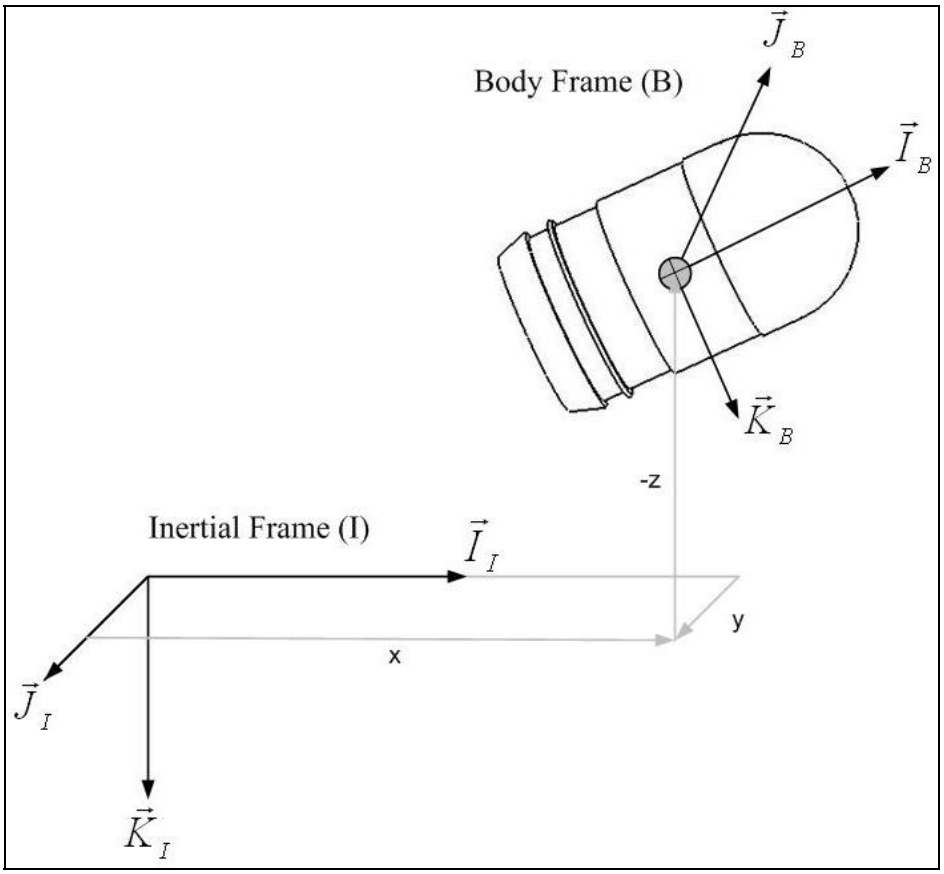

Figure 1. Reference frame and position definitions.

$$\begin{Bmatrix} \dot{p} \\ \dot{q} \\ \dot{r} \end{Bmatrix} = [I]^{-1} \left[\begin{Bmatrix} L \\ M \\ N \end{Bmatrix} - \begin{bmatrix} 0 & -r & q \\ r & 0 & -p \\ -q & p & 0 \end{bmatrix} [I] \begin{Bmatrix} p \\ q \\ r \end{Bmatrix} \right]. \tag{4}$$

Note that the total applied force components (X, Y, Z) and moment components (L, M, N) contain contributions from weight and aerodynamics. The aerodynamic portion of the applied loads in equations 3 and 4 is computed using the CFD simulation and passed to the rigid body dynamic simulation.

On the other hand, the CFD flow equations are integrated forward in time, where the motion of the projectile that drives flow dynamics is computed using the RBD algorithm. The complete set of 3-D time-dependent Navier-Stokes equations are solved in a time-accurate manner for simulation of free flight. The commercially available code, CFD++17-20, is used for the time-accurate, unsteady CFD simulations. The basic numerical framework in the code contains unified-grid, unified-physics, and unified-computing features. The 3-D, time-dependent Reynolds-averaged Navier-Stokes (RANS) equations are solved using the following finite volume equation.

$$\frac{\partial}{\partial t}\int_V W dV + \oint (F - G)\, dA = \int_V H dV\,, \tag{5}$$

where W is the vector of conservative variables, F and G are the inviscid and viscous flux vectors, respectively, H is the vector of source terms, V is the cell volume, and A is the surface area of the cell face. A second-order discretization is used for the flow variables and the turbulent viscosity equation. The turbulence closure is based on topology-parameter-free formulations. Two-equation, higher-order RANS turbulence models are used for the computation of turbulent flows. These models are ideally suited to unstructured book keeping and massively parallel processing due to their independence from constraints related to the placement of boundaries and/or zonal interfaces.

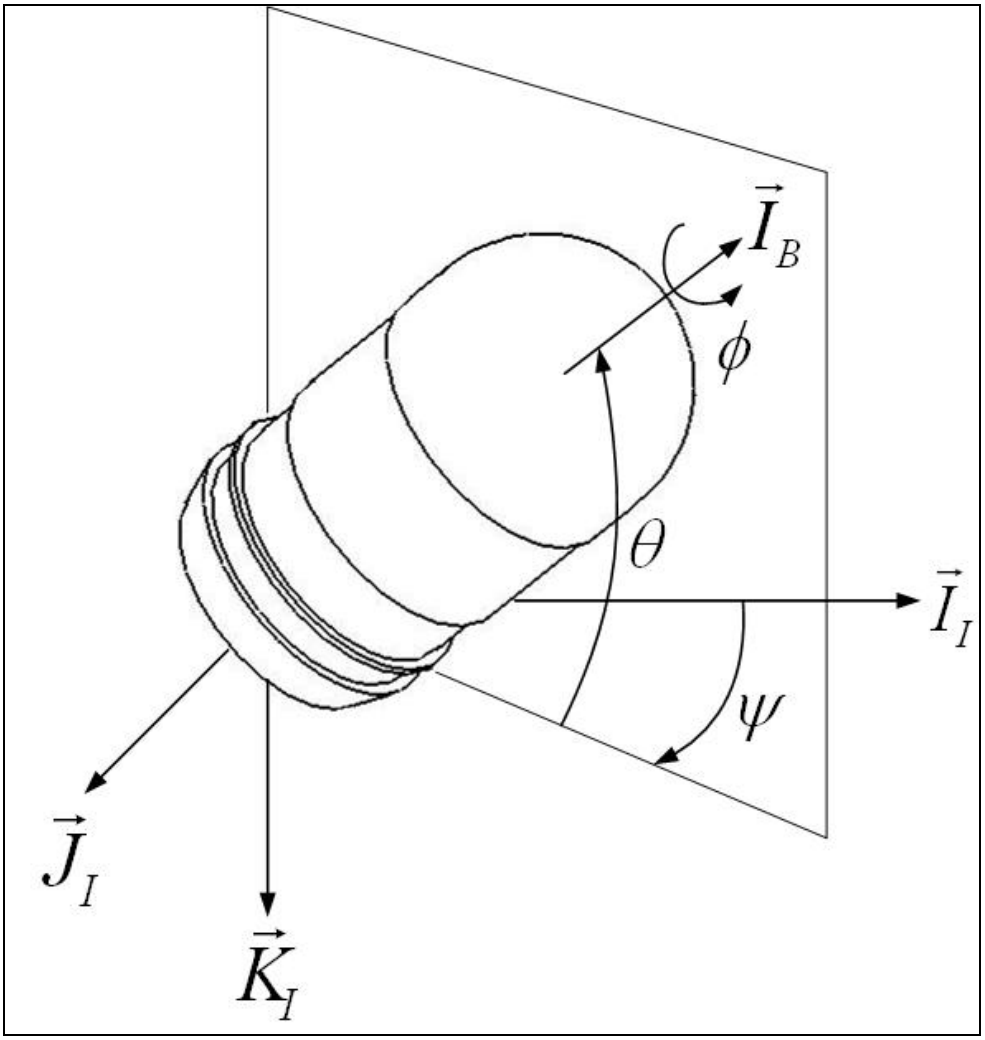

Figure 2. Projectile orientation definitions.

A dual time-stepping approach is used to integrate the flow equations to achieve the desired time accuracy. The first is an "outer" or global (and physical) time step that corresponds to the time discretization of the physical time variation term. This time step can be chosen directly by the user and is typically set to a value to represent 1/100 of the period of oscillation expected or forced in the transient flow. It is also applied to every cell and is not spatially varying. An artificial or "inner" or "local" time variation term is added to the basic physical equations. This time step and corresponding "inner-iteration" strategy is chosen to help satisfy the physical transient equations to the desired degree. For the inner iterations, the time step is allowed to vary spatially. Also, relaxation with multigrid (algebraic) acceleration is employed to reduce the residues of the physical transient equations. It is found that an order of magnitude reduction in the residues is usually sufficient to produce a good transient iteration.

The projectile in the coupled CFD/RBD simulation, along with its grid, moves and rotates as the projectile flies downrange. Grid velocity is assigned to each mesh point. For a spinning and yawing projectile, the grid speeds are assigned as if the grid is attached to the projectile and spinning and yawing with it.

In order to properly initialize the CFD simulation, two modes of operation for the CFD code are utilized, namely, an uncoupled and a coupled mode. The uncoupled mode is used to initialize the CFD flow solution, while the coupled mode represents the time-accurate coupled CFD/RBD solution. In the uncoupled mode, the rigid body dynamics are specified. The uncoupled mode begins with a computation performed in "steady-state mode," with the grid velocities prescribed to account for the proper initial position (x_0, y_0, z_0), orientation (ϕ_0, θ_0, ψ_0), and translational velocity (u_0, v_0, w_0) components of the complete set of initial conditions to be prescribed. After the quasi-steady-state solution is converged, the initial spin rate (p_0) is included and a new quasi-steady-state solution is obtained. A sufficient number of time steps are performed so that the angular orientation for the spin axis corresponds to the prescribed initial conditions. This steady-state flow solution is the starting point for the coupled solution. For the coupled solution, the mesh is translated back to the desired initial position (x_0, y_0, z_0) and the remaining angular velocity initial conditions (q_0, r_0) are then added. In the coupled mode, the aerodynamic forces and moments are passed to the RBD simulation which propagates the rigid state of the projectile forward in time.

3. Flight Dynamics Projectile Aerodynamic Model

The applied loads in equations 3 and 4 are expressed in the body reference frame and split into contributions due to weight and body aerodynamic force as shown in the following:

$$\begin{Bmatrix} X \\ Y \\ Z \end{Bmatrix} = W \begin{Bmatrix} -s_\theta \\ s_\phi c_\theta \\ c_\phi c_\theta \end{Bmatrix} - \frac{\pi}{8} \rho V^2 D^2 \begin{Bmatrix} C_{X0} + C_{X2}(v^2 + w^2)/V^2 \\ C_{NA} v/V - \frac{pD}{2V} C_{YPA} w/V \\ C_{NA} w/V + \frac{pD}{2V} C_{YPA} v/V \end{Bmatrix}. \quad (6)$$

The air loads can be further split into a steady air loads component that acts at the center of pressure and a Magnus air loads component that acts at the center of Magnus. The terms containing C_{YPA} constitute the Magnus air loads component, while the terms containing C_{X0}, C_{X2}, C_{NA} define the loads acting at the center of pressure. The externally applied moment about the projectile mass center is composed of an unsteady aerodynamic moment, along with terms, due to the fact that the center of pressure and center of Magnus are not located at the mass center.

$$\begin{Bmatrix} L \\ M \\ N \end{Bmatrix} = \frac{\pi}{8} \rho V^2 D^3 \begin{Bmatrix} C_{LDD} + \frac{pD}{2V} C_{LP} \\ C_{MA} \frac{w}{V} + \frac{qD}{2V} C_{MQ} + \frac{pD}{2V} C_{NPA} \frac{v}{V} \\ -C_{MA} \frac{v}{V} + \frac{rD}{2V} C_{MQ} + \frac{pD}{2V} C_{NPA} \frac{w}{V} \end{Bmatrix}. \quad (7)$$

The terms involving C_{MA} accounts for the center of pressure being located off the mass center, while the terms involving C_{NPA} accounts for the center of Magnus being located off the mass center. In equations 1 and 2, the aerodynamic coefficients and the distances from the aerodynamic force components to the projectile mass center are all a function of local Mach number. Typically, in flight dynamic trajectory computer codes, this dependence on Mach numbers is handled through a table look-up scheme.

4. Aerodynamic Coefficient Estimation

The time-accurate coupled CFD/RBD simulation provides a full flow solution, including the aerodynamic portion of the total applied force and moment (X, Y, Z, L, M, N), along with the full state of the rigid projectile ($x, y, z, \phi, \theta, \psi, u, v, w, p, q, r$) at each time step in the solution. The rigid state of the projectile is used to obtain the weight portion of the applied force so that the aerodynamic force can be isolated. Using the information provided by the coupled CFD/RBD simulation, it is desired to compute all aerodynamic coefficients: $C_{X0}, C_{X2}, C_{NA}, C_{YPA}$, $C_{LDD}, C_{LP}, C_{MA}, C_{MQ}, C_{NPA}$. For a fin-stabilized projectile, the Magnus force and moment are usually sufficiently small so that C_{YPA} and C_{NPA} are set to zero and removed from the fitting procedure as described next.

To estimate the aerodynamic coefficients near a particular Mach number, a set of n time accurate coupled CFD/RBD simulations are created over a relatively short time period. The initial conditions for the set of n time histories are generated to produce a rich database of aerodynamic loads and projectile states so that a unique solution can be obtained for the aerodynamic coefficients. The initial conditions for the rigid projectile states are Gaussian random numbers, with a mean and standard deviation selected to cover normal operating conditions for the projectile. Since the aerodynamic coefficients to be estimated depend on local Mach number, the set of n time histories is repeated at m different Mach numbers of interest. Thus a total of $n*m$ short time-accurate coupled CFD/RBD trajectories are generated to support computation of a complete set of aerodynamic coefficients for flight dynamic simulation.

Since initial conditions for a given set of n time histories are randomly generated and because Mach number changes during a simulation, Mach number varies slightly even for a set of time histories intended to be generated at a particular Mach number. Hence, at a particular Mach number, all aerodynamic coefficients are assumed to vary linearly with Mach number. For a general aerodynamic coefficient, this variation takes the form shown in equation. Therefore parameters at intermediate values of Mach number were linearly interpolated as shown,

$$C(M) = C_{-} + \frac{M - M_{-}}{M_{+} - M_{-}}\left(C_{+} - C_{-}\right), \tag{8}$$

where C_{-} and C_{+} are the aerodynamic coefficient values at Mach numbers slightly less than (M_{-}) and slightly greatly than (M_{+}) the target Mach number. This general form for the aerodynamic coefficients is then substituted into the aerodynamic force and moment equations. Note that all aerodynamic coefficients that are to be estimated appear in the force and moment equations in a linear fashion, suggesting a linear least-squares approach to estimate the aerodynamic coefficients at each Mach number.

Define the vectors P_X, P_{YZ}, P_L, and P_{MN} as vectors containing all the unknown aerodynamic coefficients that are to be estimated at a given target Mach number.

$$P_X = \left[C_{X0}^{-} \quad C_{X0}^{+} \quad C_{X2}^{-} \quad C_{X2}^{+} \right]. \tag{9}$$

$$P_{YZ} = \left[C_{NA}^{-} \quad C_{NA}^{+} \quad C_{YPA}^{-} \quad C_{YPA}^{+} \right]. \tag{10}$$

$$P_L = \left[C_{LP}^{-} \quad C_{LP}^{+} \quad C_{LDD}^{-} \quad C_{LDD}^{+} \right]. \tag{11}$$

$$P_{MN} = \left[C_{MA}^{-} \quad C_{MA}^{+} \quad C_{MQ}^{-} \quad C_{MQ}^{+} \quad C_{NPA}^{-} \quad C_{NPA}^{+} \right]. \tag{12}$$

Denote the total number of unknowns as j. For a fin-stabilized projectile, $j = 14$, while for a spin-stabilized projectile, $j = 18$. Assuming each time history contains k time simulation output points, then $k*n$ linear equations in j unknowns are generated at each target Mach number.

$$A_X P_X = B_X . \tag{13}$$

$$A_{YZ} P_{YZ} = B_{YZ} . \tag{14}$$

$$A_L P_L = B_L . \tag{15}$$

$$A_{MN} P_{MN} = B_{MN} . \tag{16}$$

Provided the matrices A_X, A_{YZ}, A_L, and A_{MN} are maximal rank, a unique solution for P_X, P_{YZ}, P_L, and P_{MN} exists. Thus, properties of these matrices, such as the rank or singular values, can be used as an indicator of the suitability of the CFD/RBD simulation data in estimating the aerodynamic coefficients at the target Mach number.

5. Results

In order to exercise the previously developed method, a detailed comparison of the aerodynamic forces and moments for a typical finned projectile are shown in figures 3–8. Mach number varied from 3.03 to 2.97, covering 0.07 s and containing 3317 points. The projectile had the following properties: mass of 4.84×10^{-1} kg, length of 1.259×10^{-1} m, diameter of 1.319×10^{-2} m, and axial inertia of 7.4×10^{-7} kg-m^2. The estimated data is generated using equations 5 and 6 with the identified aerodynamic coefficients. Aerodynamic forces and moments agree well, particularly the Y and Z components, which appear coincident in the plotted data. The CFD/RBD data appears slightly noisy in both the axial force and rolling moment. However, the estimated data removes the noise.

Figures 9–17 present estimation results for an example of a finned projectile and an example of a spin-stabilized projectile. The finned projectile is a 120-mm direct-fire kinetic energy round, while the spin-stabilized projectile is a 155-mm shell. Synthetic CFD/RBD data was generated using a rigid 6 degree-of-freedom trajectory simulation. The solid lines correspond to the coefficient values used to generate the synthetic CFD/RBD data. The “square” symbols represent the finned projectile aerodynamic coefficient estimations, and the “circle” symbols represent the spin-stabilized aerodynamic coefficient estimations. In figure 13, Cmq values for the finned projectile are scaled by a factor of 1/40, so that data for both rounds is easily viewed. The spin-stabilized projectile covers a Mach range from 0.6 to 4, while the finned projectile covers a Mach range from 1 to 4. One-thousand output points were used from each of the 25 runs at each Mach number of interest. For the finned projectile, each run had random initial conditions for angular rates with a zero mean, and a Gaussian standard deviation of 3 rad/s for roll rate and 2 rad/s for pitch and yaw rates. For the spin-stabilized projectile, each run had random initial conditions for roll rate, with a mean value of 900 rad/s and Gaussian standard deviation of 10 rad/s.

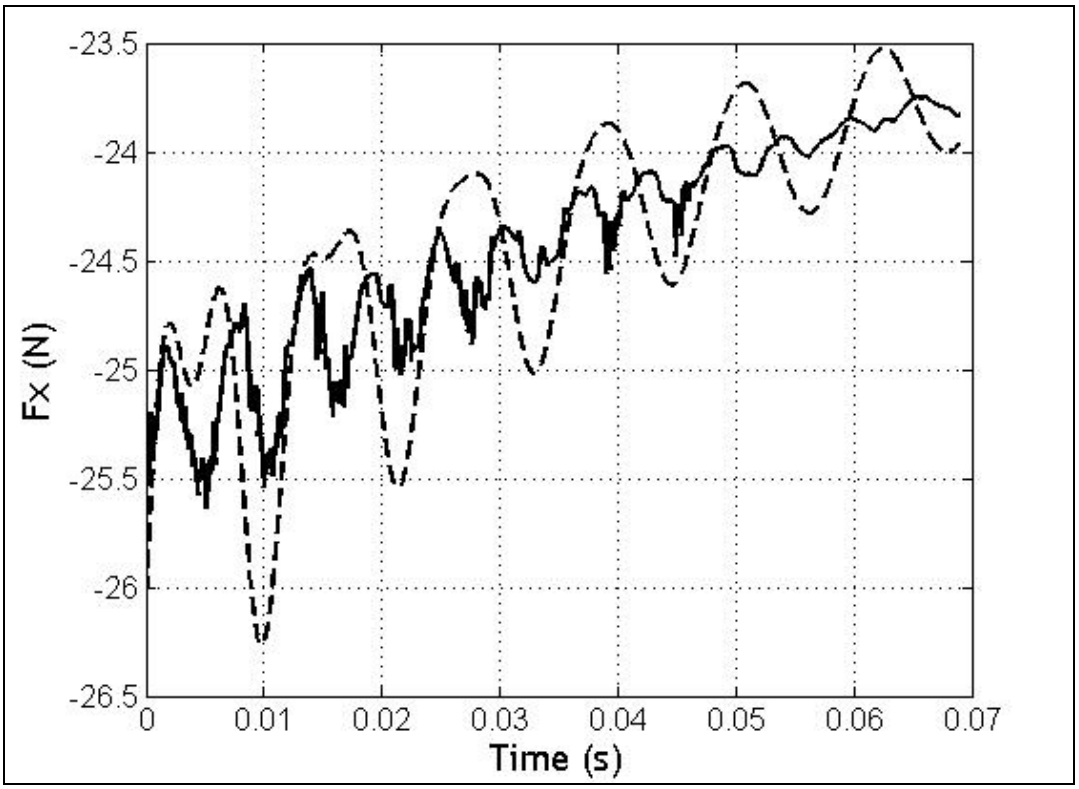

Figure 3. Estimated (dashed) and CFD/RBD (solid) body axis axial force vs. time.

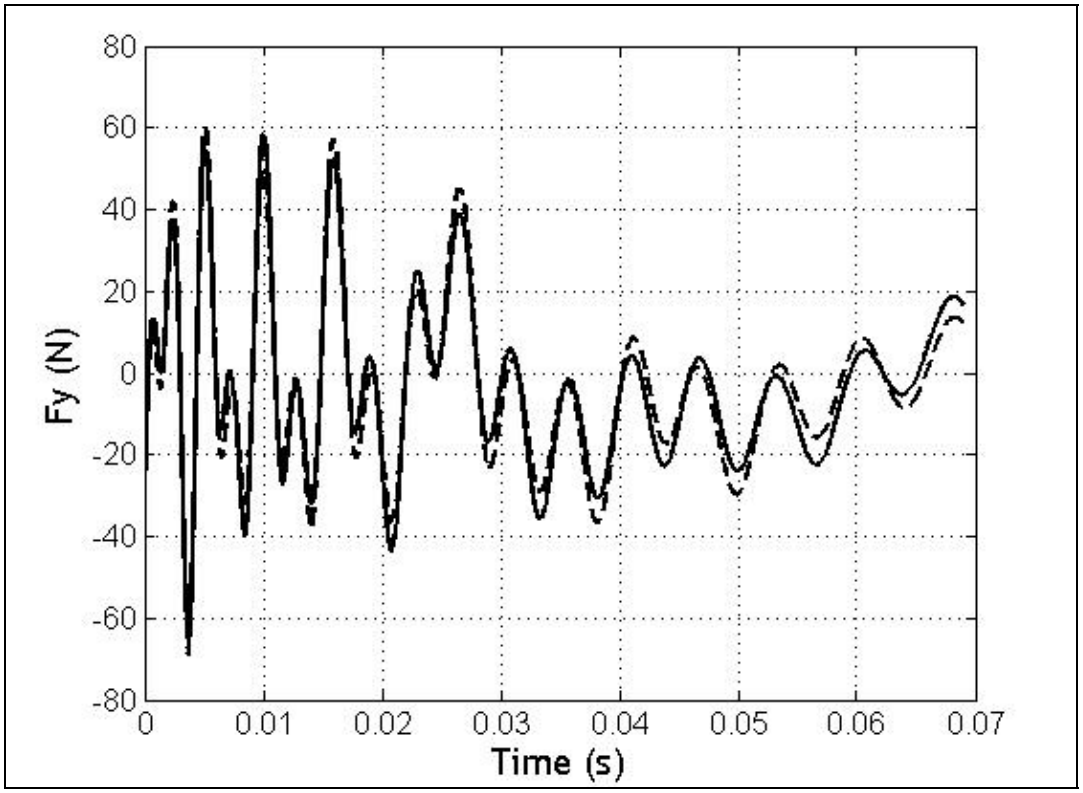

Figure 4. Estimated (dashed) and CFD/RBD (solid) body axis side force vs. time.

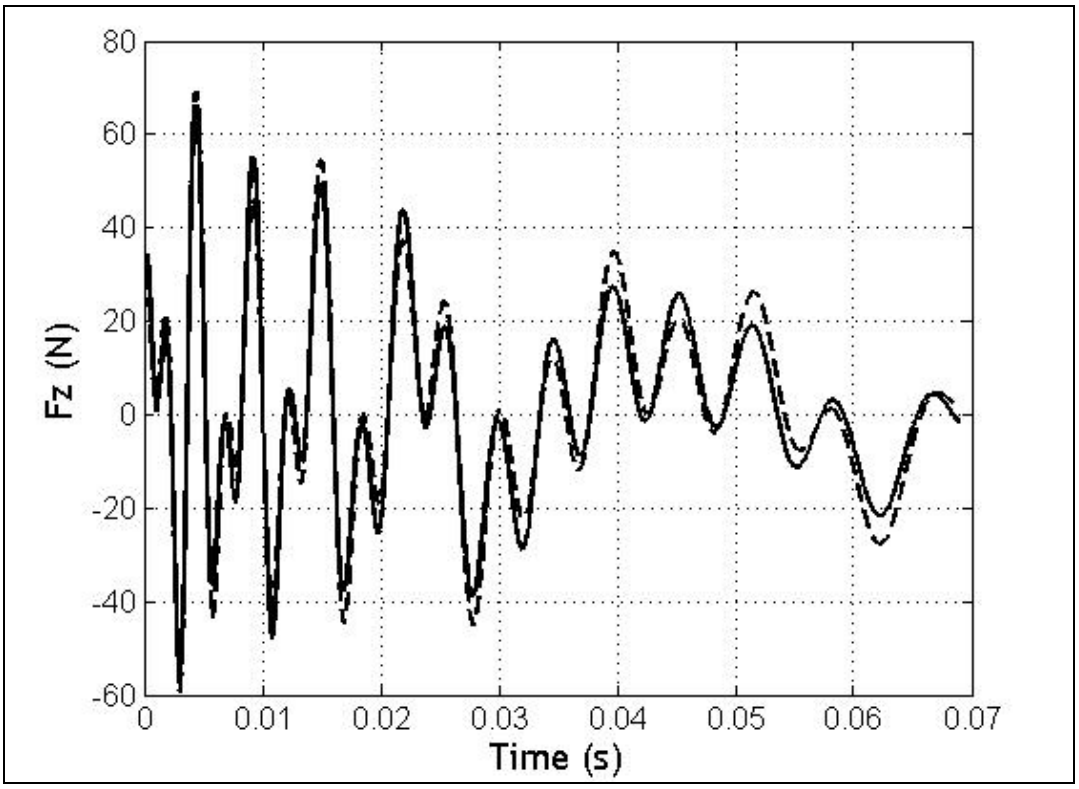

Figure 5. Estimated (dashed) and CFD/RBD (solid) body axis vertical force vs. time.

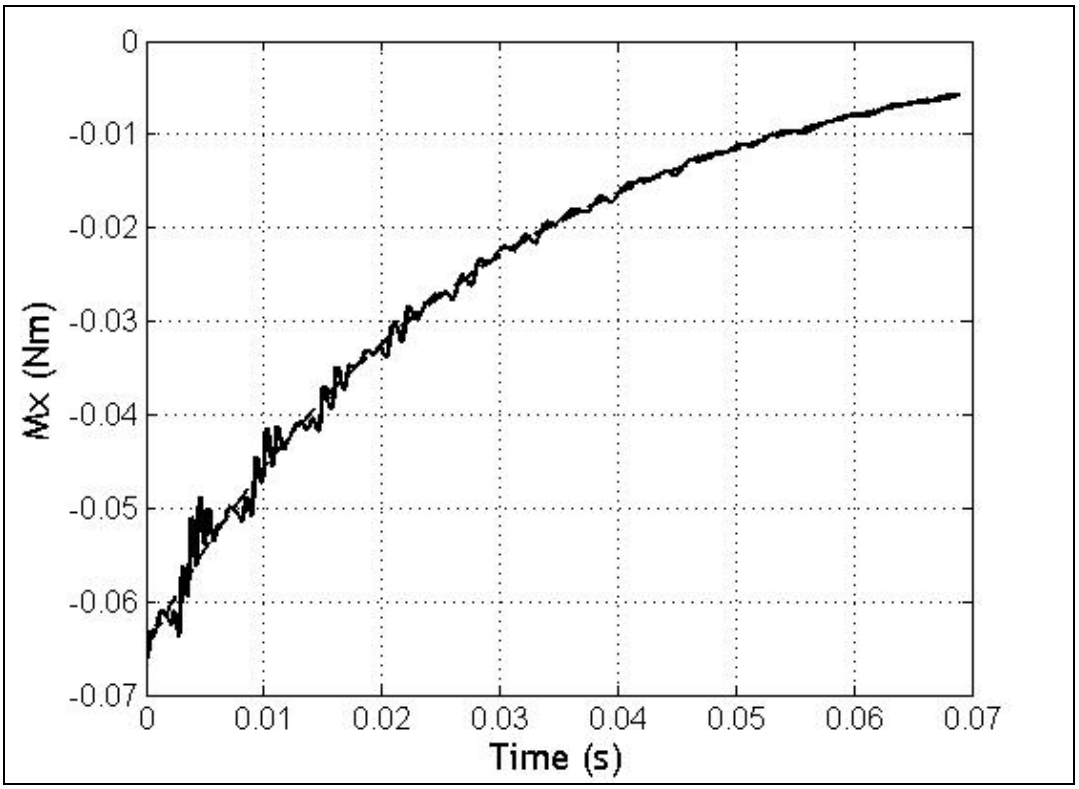

Figure 6. Estimated (dashed) and CFD/RBD (solid) body axis rolling moment vs. time.

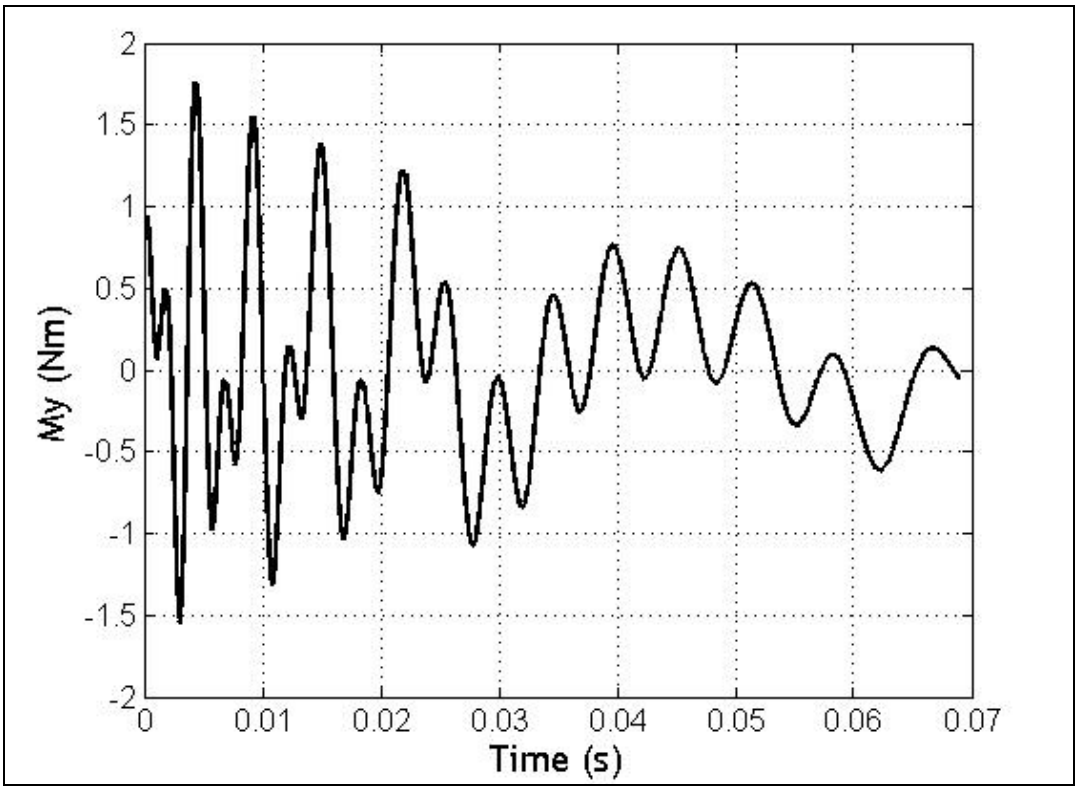

Figure 7. Estimated (dashed) and CFD/RBD (solid) pitching moment vs. time.

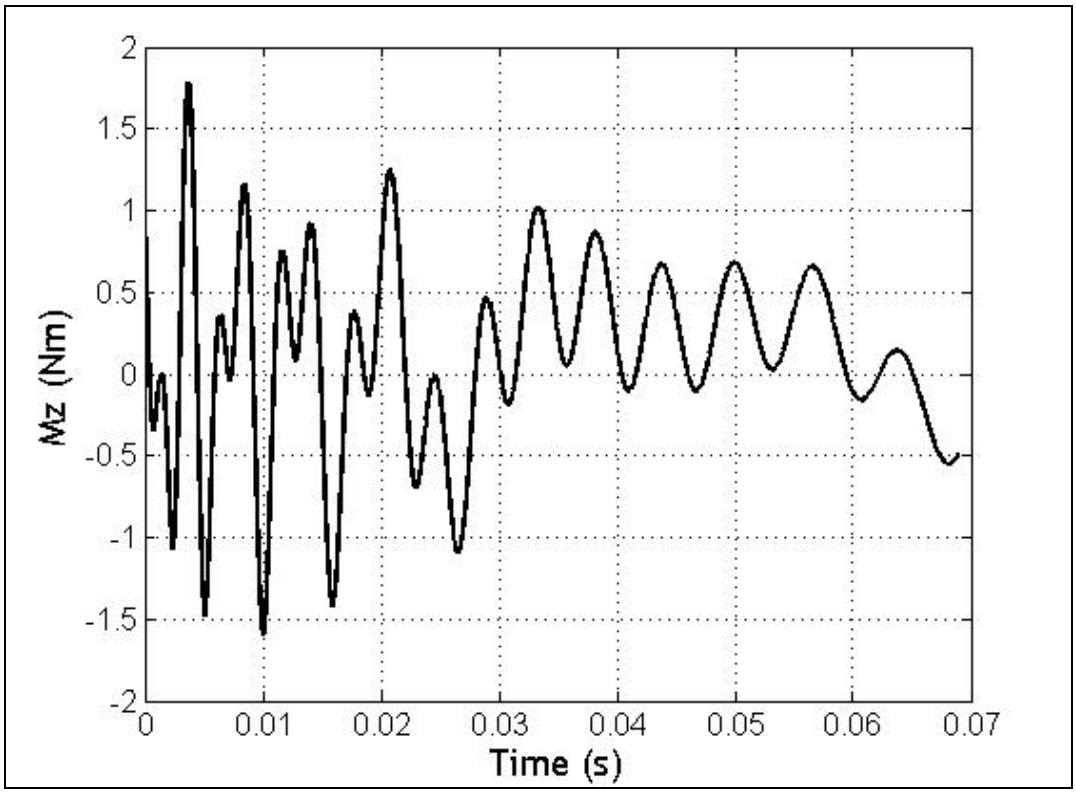

Figure 8. Estimated (dashed) and CFD/RBD (solid) yawing moment vs. time.

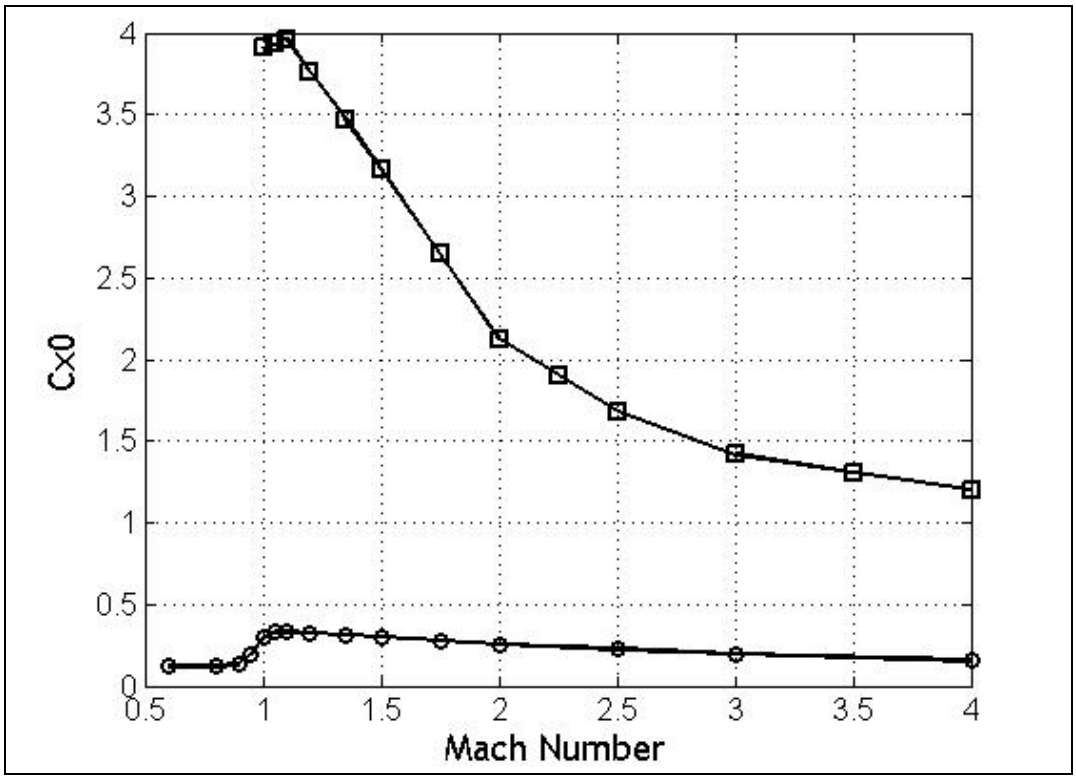

Note: square = spin-stabilized projectile, circle = finned projectile, solid line = data, and symbols = estimated.

Figure 9. CX0 vs. Mach number.

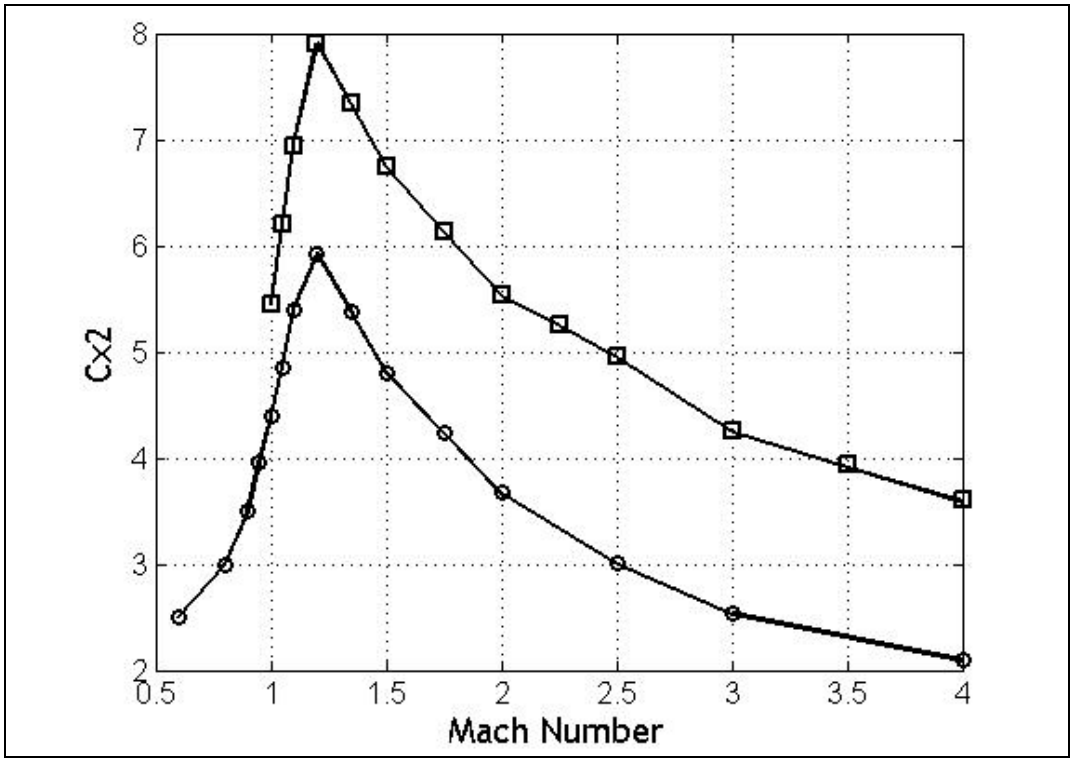

Note: square = spin-stabilized projectile, circle = finned projectile, solid line = data, and symbols = estimated.

Figure 10. CX2 vs. Mach number.

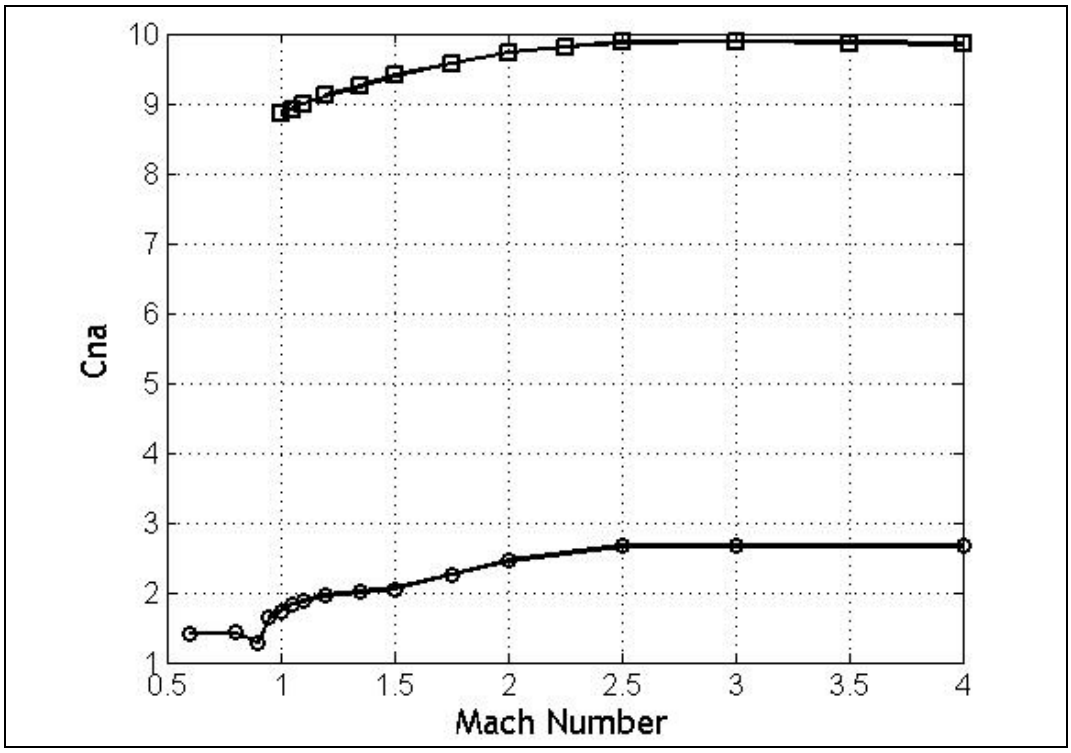

Note: square = spin-stabilized projectile, circle = finned projectile, solid line = data, and symbols = estimated.

Figure 11. CNA vs. Mach number.

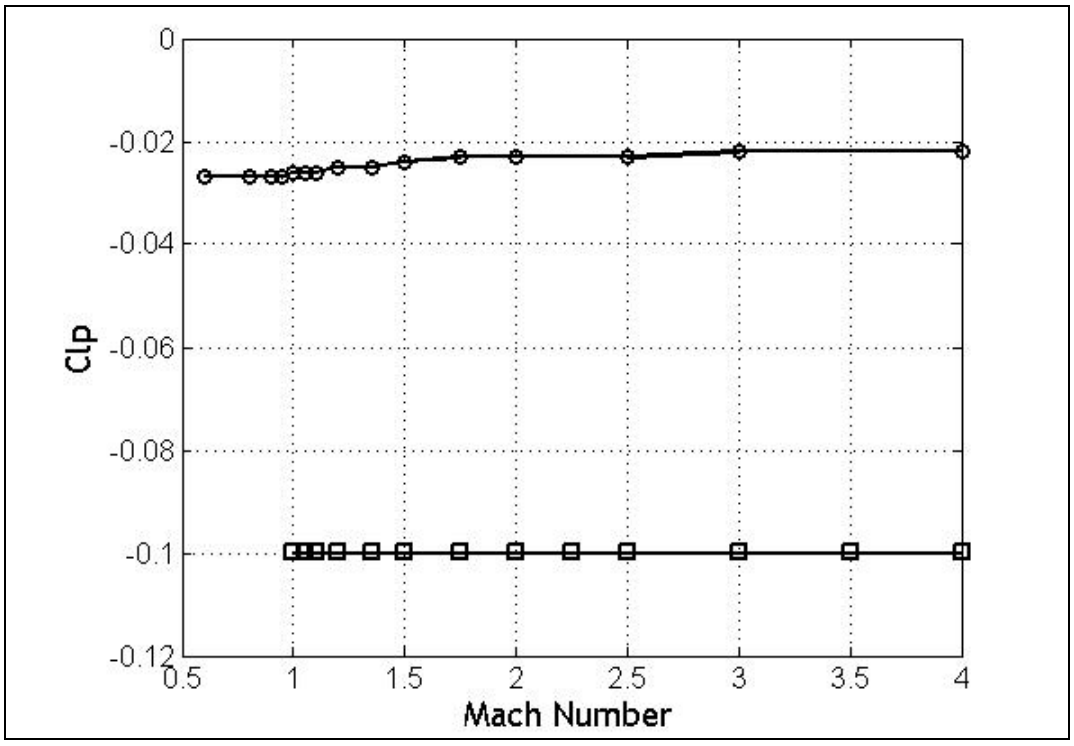

Note: square = spin-stabilized projectile, circle = finned projectile, solid line = data, and symbols = estimated.

Figure 12. CLP vs. Mach number.

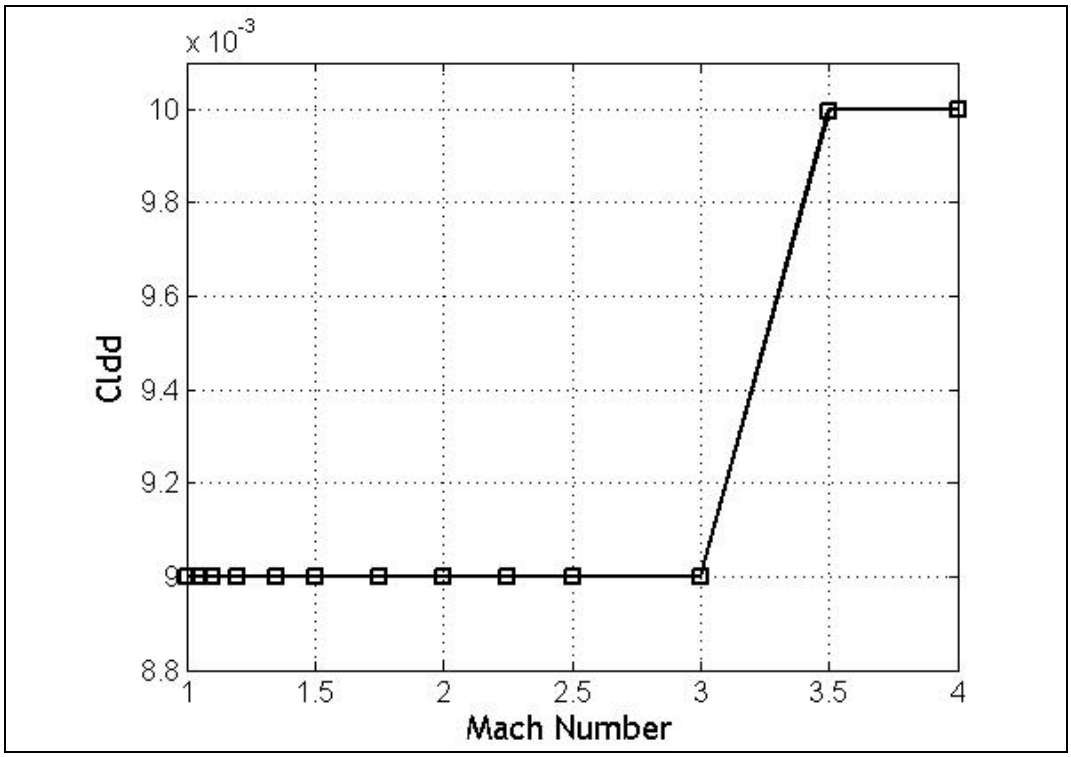

Note: square = spin-stabilized projectile, circle = finned projectile, solid line = data, and symbols = estimated.

Figure 13. CLDD vs. Mach number.

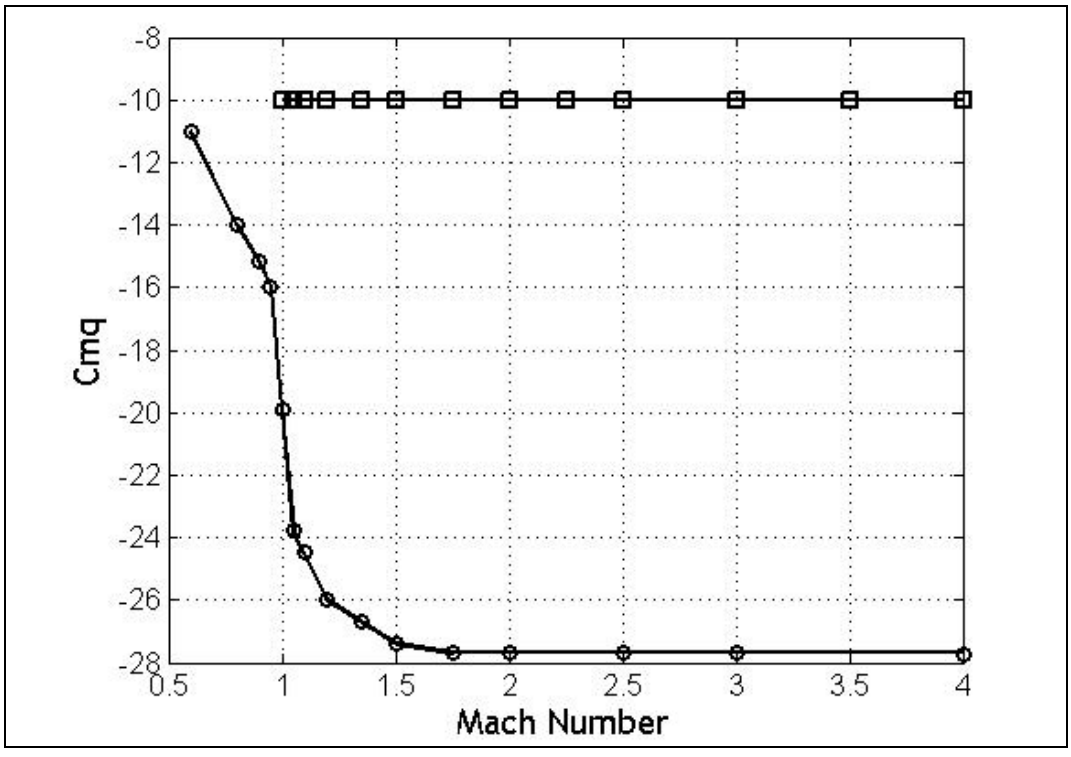

Note: square = spin-stabilized projectile, circle = finned projectile, solid line = data, and symbols = estimated.

Figure 14. CMQ vs. Mach number.

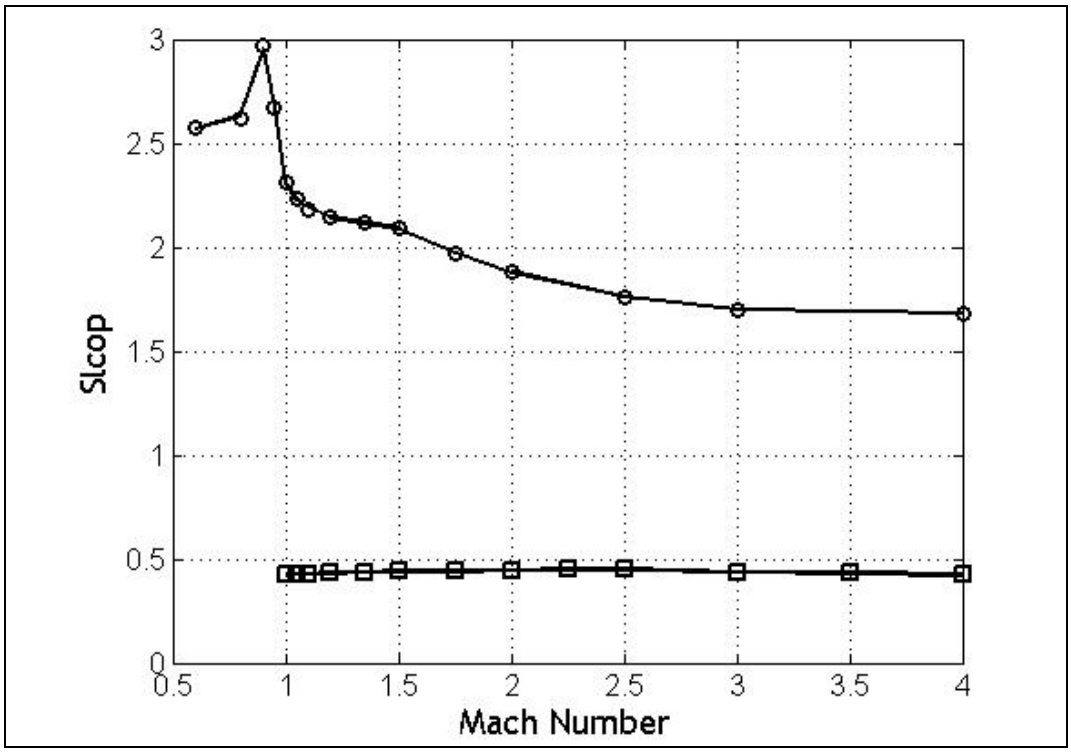

Note: square = spin-stabilized projectile, circle = finned projectile, solid line = data, and symbols = estimated.

Figure 15. Station line center of pressure vs. Mach number.

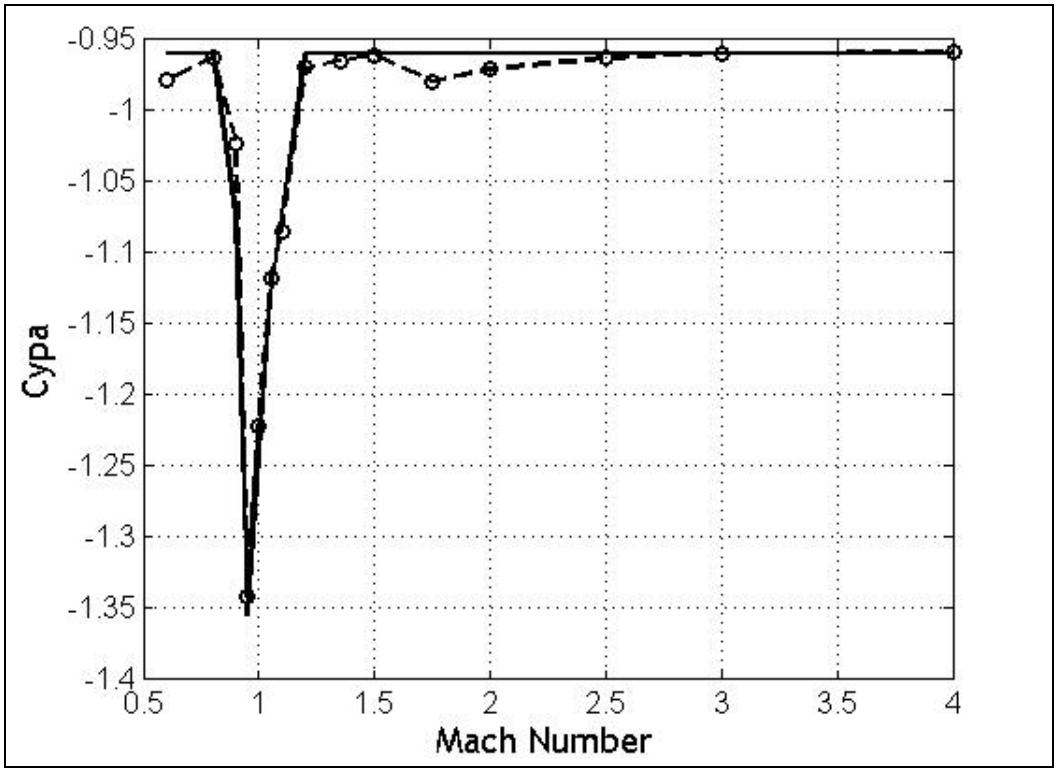

Note: dashed line = data, and symbols = estimated.

Figure 16. CYPA vs. Mach number for spin-stabilized projectile.

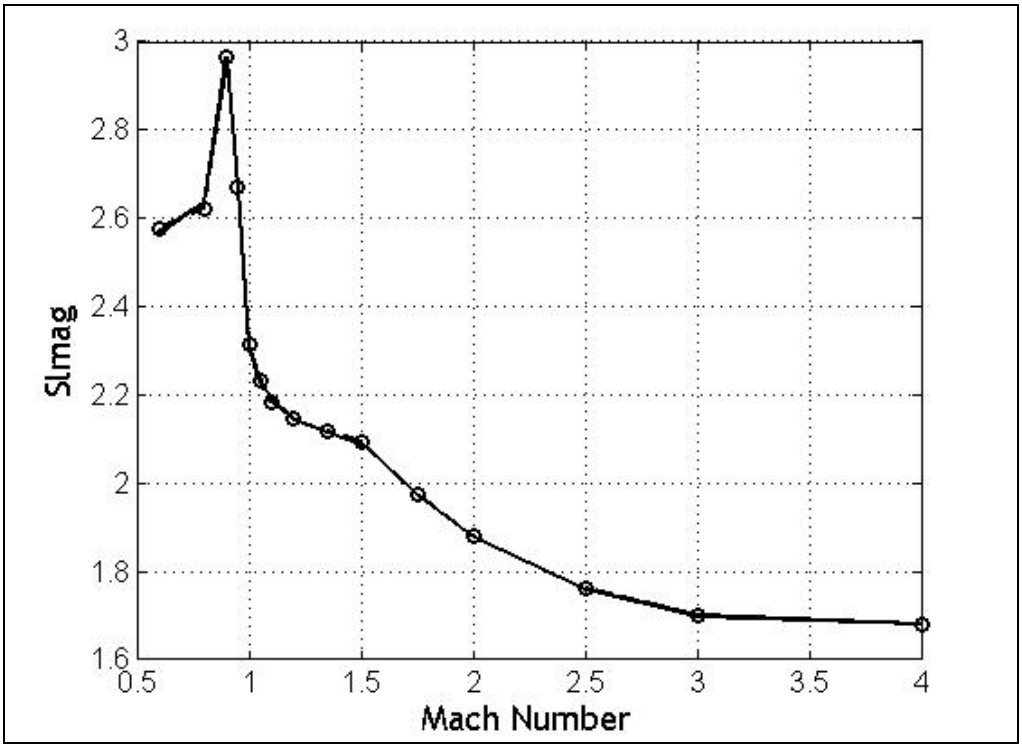

Note: solid line = data, and symbols = estimated.

Figure 17. Station line center of Magnus force vs. Mach number for spin-stabilized projectile.

Parametric trade studies were conducted to determine the effect of the number of runs needed for convergence of the aerodynamic coefficients, as well as, the effect of the length of the time snippet on convergence. Figures 18–23 present results for CX2 and CMQ as a function of the number of runs used for estimation. The number of runs at each Mach number was varied to values of 4, 6, and 10. The number of output points was one for all runs. Note that for 10 runs, the aerodynamic coefficients are converged. In figures 24 and 25, the effect of the number of data points in each time snippet is investigated. Three values are shown: 1, 2, and 5. The number of runs at each Mach number is six, and the snipet length equals 0.1 s. Note that CX2 and CMQ are both converged with five data points. While not shown, all other aerodynamic coefficients are converged as well.

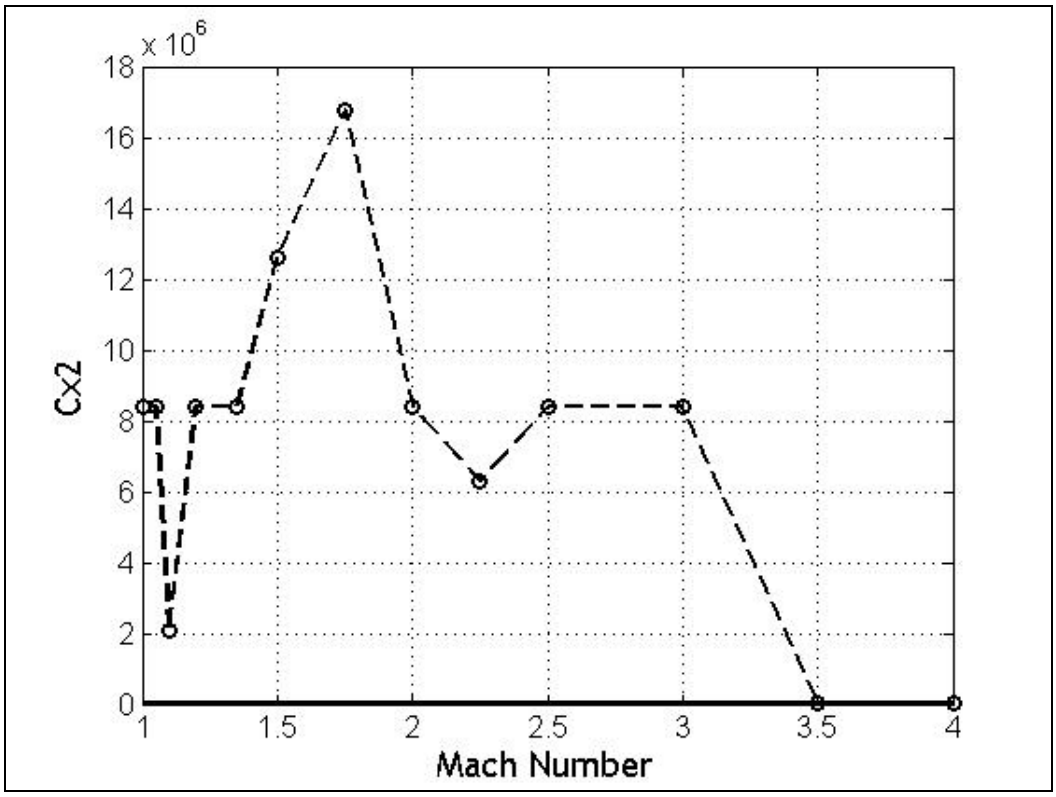

Figure 18. CX2 vs. Mach number: one data point per time snippet, four time snippets.

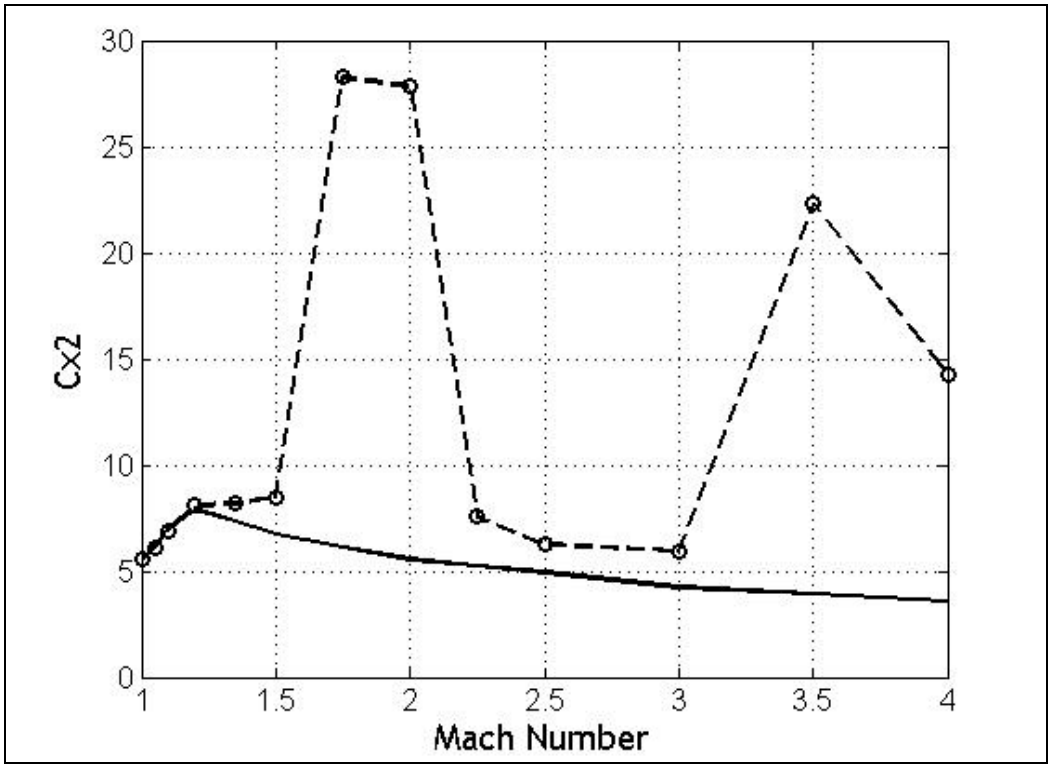

Figure 19. CX2 vs. Mach number: one data point per time snippet, six time snippets.

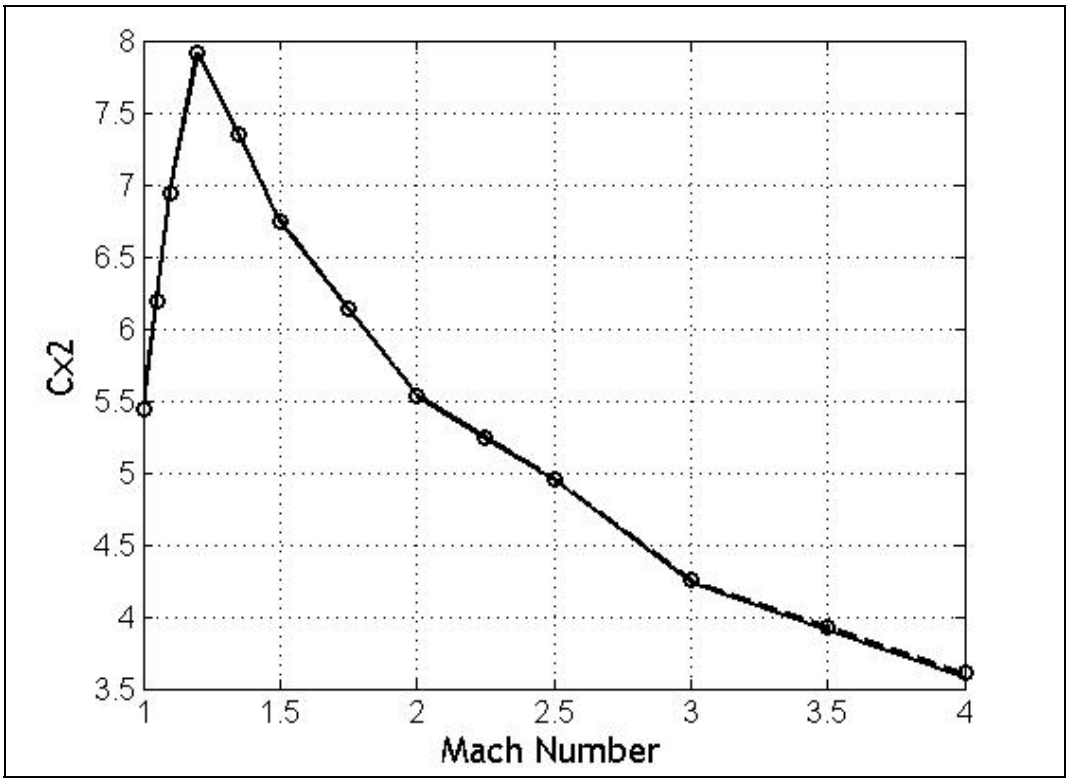

Figure 20. CX2 vs. Mach number: one data point per time snippet, 10 time snippets.

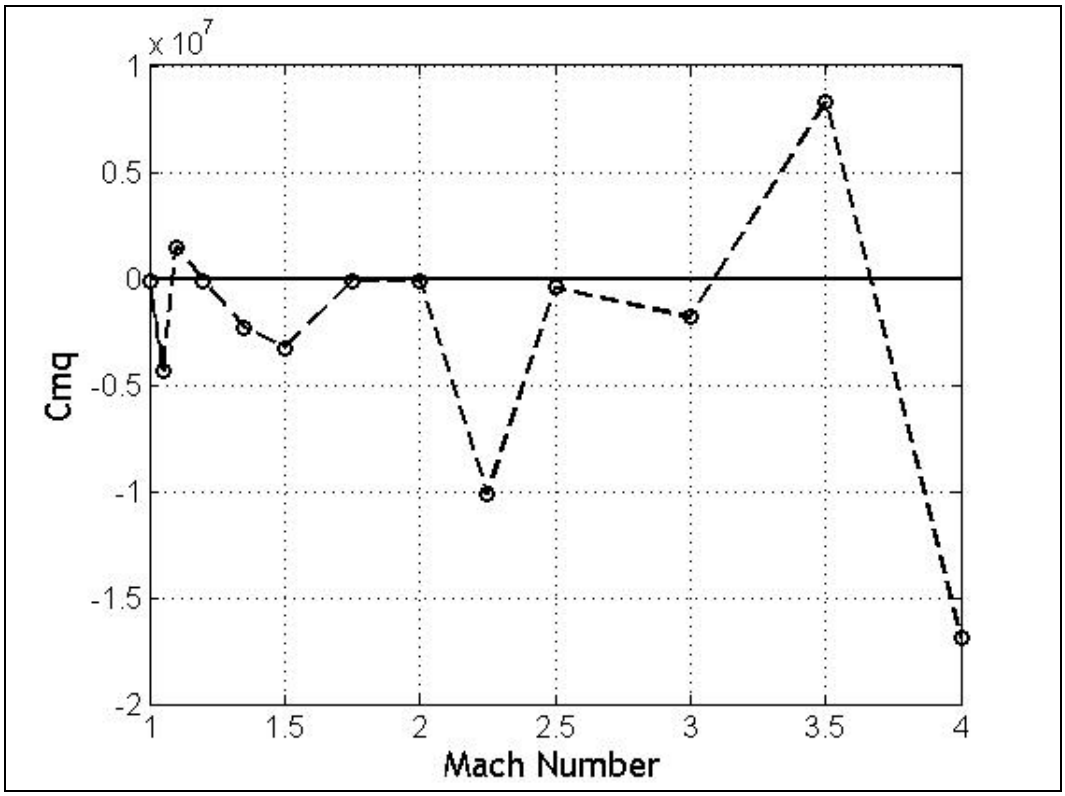

Figure 21. CMQ vs. Mach number: one data point per time snippet, four time snippets.

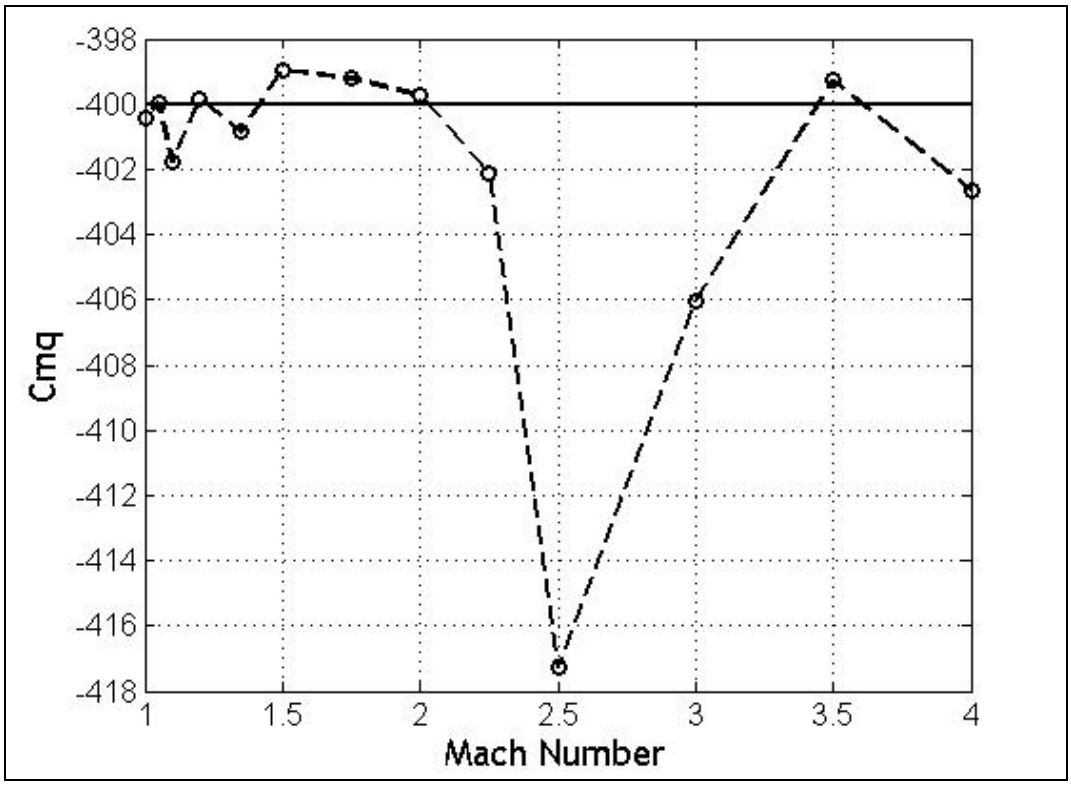

Figure 22. CMQ vs. Mach number: one data point per time snippet, six time snippets.

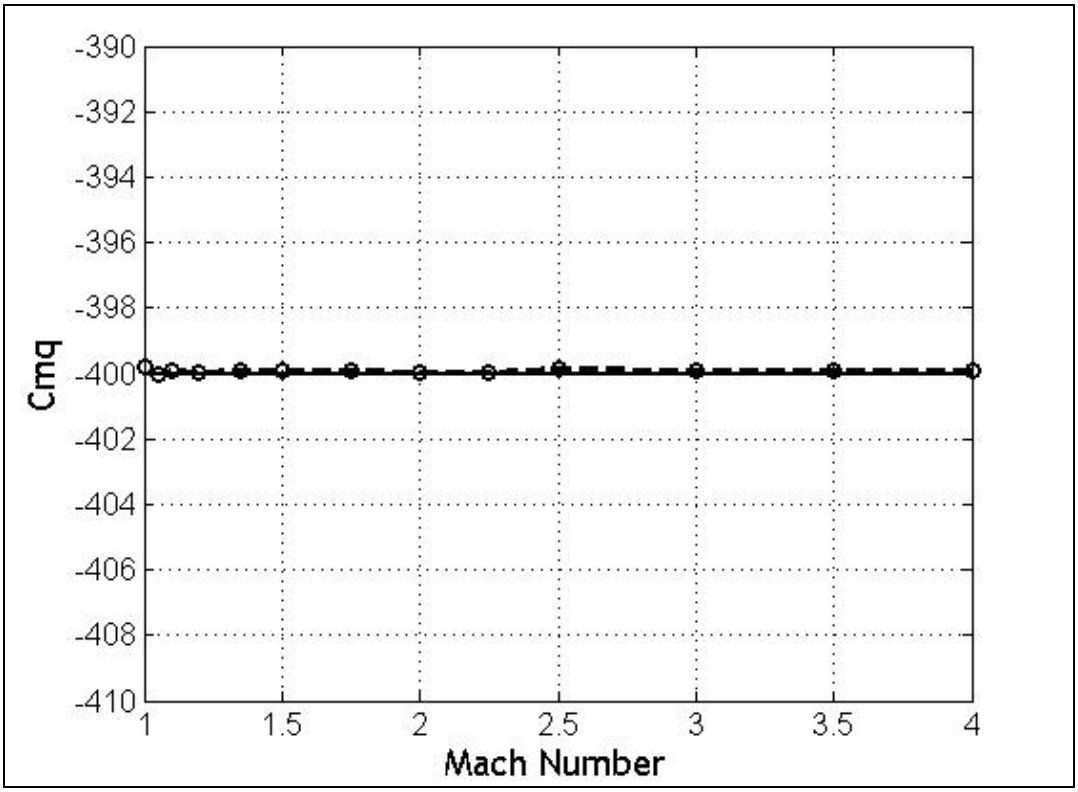

Figure 23. CMQ vs. Mach number: one data point per time snippet, 10 time snippets.

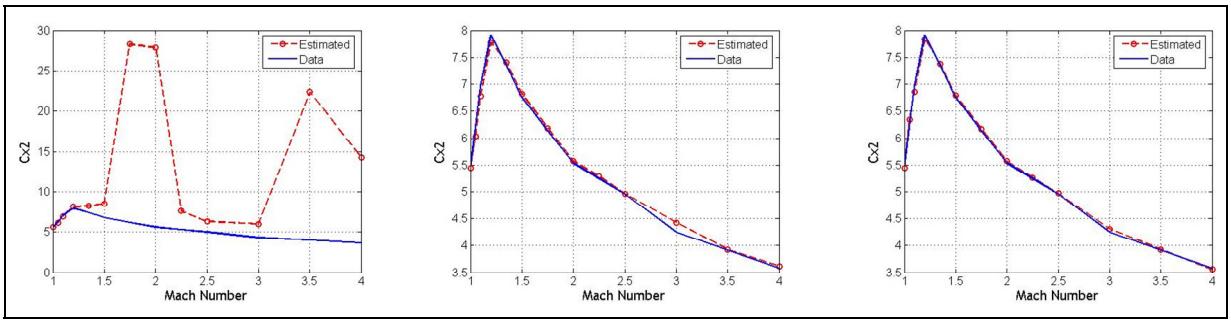

Figure 24. CX2 vs. Mach number: data points per time snippet = one (left), two (middle), five (right); time snippets = six.

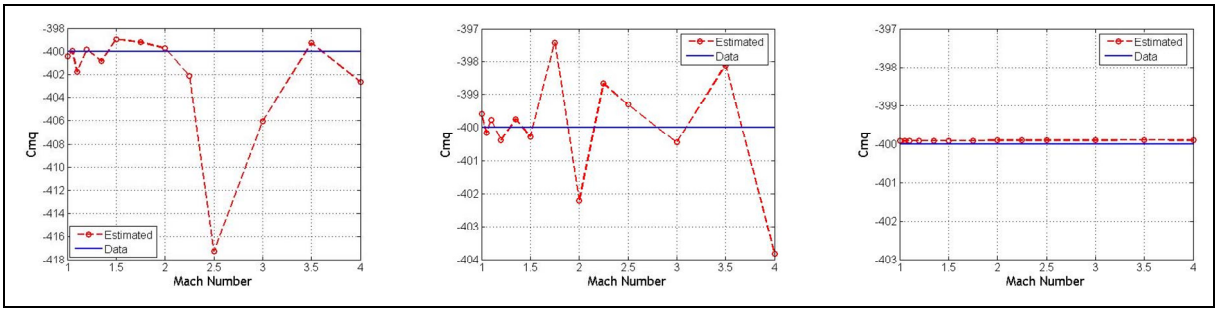

Figure 25. CMQ vs. Mach number: data points per time snippet = one (left), two (middle), five (right); time snippets = six.

6. Conclusions

Using a time-accurate, computational fluid dynamics simulation that is tightly coupled to a rigid body dynamics simulation, a method to efficiently generate a complete aerodynamic description for projectile flight dynamic modeling is described. A set of n very short time snippets of simulated projectile motion at m different Mach numbers is computed and employed as baseline data. The combined CFD/RBD analysis computes time synchronized air loads and projectile state vector information, leading to a straightforward fitting procedure to obtain the aerodynamic coefficients. The estimation procedure decouples into four subproblems that are each solved via linear least squares. By inspecting the condition number of each fitting matrix, the suitability of the time history data to predict a selected set of aerodynamic coefficients can be assessed. The overall method has been shown to work well for both fin- and spin-stabilized projectiles. As would be expected, convergence of the aerodynamic coefficients is strongly influenced by the number of time snippets and the number of points in each time snippet. This technique provides a new means for the CFD analyst to predict aerodynamic coefficients for flight dynamic simulation purposes. While CFD/RBD is computationally intensive, the method described in this report provides a means to monitor progress in estimating aerodynamic coefficients through the individual fitting matrices.

7. References

1. Sun, J.; Cummings, R. Evaluation of Missile Aerodynamic Characteristics Using Rapid Prediction Techniques. *Journal of Spacecraft and Rockets* **1984**, *21* (6), 513–520.

2. Moore, F. The 2005 Version of the Aeroprediction Code (AP05), *AIAA Atmospheric Flight Mechanics Conference*, AIAA 2004-4715, Providence, RI, 2004.

3. Sooy, T.; Schmidt, R. Aerodynamic Predictions, Comparisons, and Validations Using Missile DATCOM and Aeroprediction 98, *AIAA Aerospace Sciences Meeting and Exhibit*, AIAA-2004-1246, Reno, NV, 2004.

4. Simon, J.; Blake, W. Missile DATCOM – High Angle of Attack Capabilities, *AIAA Atmospheric Flight Mechanics Conference*, AIAA-1999-4258, Portland, OR, 1999.

5. Neely, A.; Auman, L. Missile DATCOM Transonic Drag Improvements for Hemispherical Nose Shapes, *AIAA Applied Aerodynamics Conference*, AIAA-2003-3668, Orlando, FL, 2003.

6. Blake, W. Missile DATCOM – 1997 Status and Future Plans, *AIAA Applied Aerodynamics Conference*, AIAA-1997-2280, Atlanta, GA, 1997.

7. Dupuis, A.; Berner, C. Wind Tunnel Tests of a Long Range Artillery Shell Concept, *AIAA Atmospheric Flight Mechanics Conference*, AIAA-2002-4416, Monterey, CA, 2002.

8. Berner, C.; Dupuis, A. Wind Tunnel Tests of a Grid Fin Projectile Configuration, *AIAA Aerospace Sciences Meeting*, AIAA-2001-0105, Reno, NV, 2001.

9. Evans, J. Prediction of Tubular Projectile Aerodynamics Using the ZUES Euler Code. *Journal of Spacecraft and Rockets* **1989**, *26* (5), 314–321.

10. Sturek, W.; Nietubicz, C.; Sahu, J.; Weinacht, P. Applications of Computational Fluid Dynamics to the Aerodynamics of Army Projectiles. *Journal of Spacecraft and Rockets* **1994**, *31* (2), 186–199.

11. Nusca, M.; Chakravarthy, S.; Goldberg, U. Computational Fluid Dynamics Capability for the Solid-Fuel Ramjet Projectile. *Journal of Propulsion and Power* **1990**, *6* (3).

12. Silton, S. Navier-Stokes Computations for a Spinning Projectile from Subsonic to Supersonic Speeds. *Journal of Spacecraft and Rockets* **2005**, *42* (2), 223–231.

13. DeSpirito, J.; Vaughn, M.; Washington, D. Numerical Investigation of Canard-Controlled Missile with Planar Grid Fins. *Journal of Spacecraft and Rockets* **2003**, *40* (3), 363–370.

14. Graham, M.; Weinacht, P.; Bennett, J. Numerical Investigation of Supersonic Jet Interaction for Finned Bodies. *Journal of Spacecraft and Rockets* **2000**, *37* (5), 675–683.

15. Weinacht, P. Navier-Stokes Prediction of the Individual Components of the Pitch Damping Sum. *Journal of Spacecraft and Rockets* **1998**, *35* (5), 598–605.

16. Guidos, B.; Weinacht, P.; Dolling, D. Navier-Stokes Computations for Pointed, Spherical, and Flat Tipped Shells at Mach 3. *Journal of Spacecraft and Rockets* **1992**, *29* (3), 305–311.

17. Weinacht, P.; Sturek, W. Computation of the Roll Characteristics of a Finned Projectile. *Journal of Spacecraft and Rockets* **1996**, *33* (6) 769–775.

18. Park, S.; Kwon, J. Navier-Stokes Computations of Stability Derivatives for Symmetric Projectiles, *AIAA Aerospace Sciences Meeting*, AIAA-2004-0014, Reno, NV, 2004.

19. Qin, N.; Ludlow, K.; Shaw, S.; Edwards, J.; Dupuis, A. Calculation of Pitch Damping for a Flared Projectile. *Journal of Spacecraft and Rockets* **1997**, *34* (4), 566–568.

20. Weinacht, P. Coupled CFD/GN&C Modeling for a Smart Material Canard Actuator, *AIAA Atmospheric Flight Mechanics Conference*, AIAA-2004-4712, Providence, RI, 2004.

21. Park, S.; Kim, Y.; Kwon, J. Prediction of Dynamic Damping Coefficients Using Unsteady Dual Time Stepping Method, *AIAA Aerospace Sciences Meeting*, AIAA-2002-0715, Reno, NV, 2002.

22. DeSpirito, J.; Heavey, K. CFD Computation of Magnus Moment and Roll-Damping Moment of a Spinning Projectile, *AIAA Atmospheric Flight Mechanics Conference*, AIAA-2004-4713, Providence, RI, 2004.

23. Garon, K.; Abate, G.; Hathaway, W. Free-Flight Testing of a Generic Missile With MEMs Protuberances, *AIAA Aerospace Sciences Meeting*, AIAA-2003-1242, Reno, NV, 2003.

24. Kruggel, B. High Angle of Attack Free Flight Missile Testing, *AIAA Aerospace Sciences Meeting*, AIAA-1999-0435, Reno, NV, 1999.

25. Danberg, J.; Sigal, A.; Clemins, I. Aerodynamic Characteristics of a Family of Cone-Cylinder-Flare Projectiles. *Journal of Spacecraft and Rockets* **1990**, *27* (4).

26. Dupuis, A. Free-Flight Aerodynamic Characteristics of a Practice Bomb at Subsonic and Transonic Velocities, *AIAA Atmospheric Flight Mechanics Conference*, AIAA-2002-4414, Monterey, CA, 2002.

27. Abate, G.; Duckerschein, R.; Hathaway, W. Subsonic/transonic Free-Flight Tests of a Generic Missile With Grid Fins, *AIAA Aerospace Sciences Meeting*, AIAA-2000-0937, Reno, NV, 2000.

28. Chapman, G.; Kirk, D. A Method for Extracting Aerodynamic Coefficients From Free-Flight Data, *AIAA Journal*, **1970**, *8* (4), 753–758.

29. Abate, G.; Klomfass, A. Affect Upon Aeroballistic Parameter Identification From Flight Data Errors, *AIAA Aerospace Sciences Meeting*, Reno, NV, 2005.

30. Abate, G.; Klomfass, A. A New Method for Obtaining Aeroballistic Parameters From Flight Data, *Aeroballistic Range Association Meeting*, Freiburg, Germany, 2004.

31. Weinacht, P.; Sturek, W.; Schiff, L. Projectile Performance, Stability, and Free-Flight Motion Prediction Using Computational Fluid Dynamics. *Journal of Spacecraft and Rockets* **2004**, *41* (2), 257–263.

32. Sahu, J. Time-Accurate Numerical Prediction of Free-Flight Aerodynamics of a Finned Projectile, *AIAA Atmospheric Flight Mechanics Conference*, AIAA-2005-5817, San Francisco, CA, 2005.

List of Symbols, Abbreviations, and Acronyms

x, y, z	Components of position vector of mass center in an inertial reference frame
ϕ, θ, ψ	Euler roll, pitch, and yaw angles of box
u, v, w	Components of velocity vector of mass center in body reference frame
p, q, r	Components of angular velocity vector in body reference frame
F_x, F_y, F_z	Total applied force components in body reference frame
M_x, M_y, M_z	Total applied moment components about mass center in body reference frame
V	Magnitude of relative aerodynamic velocity vector of mass center
ρ	Air density
D	Projectile diameter
α	Aerodynamic angle of attack
C_{x0}	Zero yaw drag aerodynamic coefficient
C_{x2}	Yaw drag aerodynamic coefficient
C_{na}	Normal force due to angle of attack aerodynamic coefficient
C_{ypa}	Magnus force aerodynamic coefficient
C_{lp}	Roll damping aerodynamic coefficient
C_{ldd}	Fin cant aerodynamic coefficient
C_{mq}	Pitch damping moment aerodynamic coefficient
D_{cop}	Distance from the mass center to the center of pressure
D_{mag}	Distance from the mass center to the center of Magnus
CFD	Computational fluid dynamics
RANS	Reynolds-averaged Navier-Stokes
RBD	Rigid body dynamic
3-D	Three-dimensional

NO. OF COPIES	ORGANIZATION
1 (PDF ONLY)	DEFENSE TECHNICAL INFORMATION CTR DTIC OCA 8725 JOHN J KINGMAN RD STE 0944 FORT BELVOIR VA 22060-6218
1	US ARMY RSRCH DEV & ENGRG CMD SYSTEMS OF SYSTEMS INTEGRATION AMSRD SS T 6000 6TH ST STE 100 FORT BELVOIR VA 22060-5608
1	DIRECTOR US ARMY RESEARCH LAB IMNE ALC IMS 2800 POWDER MILL RD ADELPHI MD 20783-1197
3	DIRECTOR US ARMY RESEARCH LAB AMSRD ARL CI OK TL 2800 POWDER MILL RD ADELPHI MD 20783-1197

ABERDEEN PROVING GROUND

1	DIR USARL AMSRD ARL CI OK TP (BLDG 4600)

NO. OF COPIES ORGANIZATION

1 US AIR FORCE RSRCH LAB
MUNITIONS DIR
AFRL/MNAV
G ABATE
101 W EGLIN BLVD
STE 219
EGLIN AFB FL 32542

5 GEORGIA INSTITUTE OF TECHLGY
DEPT OF AEROSPACE ENGRNG
M COSTELLO
ATLANTA GA 30332

1 CDR US ARMY ARDEC
AMSTA AR CCH
S MUSALI
PICATINNY ARSENAL NJ
07806-5000

2 CDR
US ARMY TANK MAIN
ARMAMENT SYSTEM
AMCPM TMA
D GUZIEWICZ
C LEVECHIA
PICATINNY ARSENAL NJ
08706-5000

1 CDR USARDEC
AMSTA AR CCH A
M PALATHINGAL
PICATINNY ARSENAL NJ
07806-5000

1 CDR US ARMY RES OFC
AMXRO RT IP TECH LIB
PO BOX 12211
RESEARCH TRIANGLE PARK NJ
27709-2211

3 ARROW TECH ASSOC INC
R WHYTE
A HATHAWAY
H STEINHOFF
1233 SHELBOURNE RD STE D8
SOUTH BURLINGTON VT 05403

NO. OF COPIES ORGANIZATION

ABERDEEN PROVING GROUND

30 DIR USARL
AMSRD ARL HR SD
T MERMAGEN
AMSRD ARL WM EG
E SCHMIDT
AMSRD ARL WM B
R COATES
AMSRD ARL WM BA
G BROWN
B DAVIS
T HARKINS
T KOGLER
D LYON
S WANSACK
M WILSON
AMSRD ARL WM BC
I CELMINS
M CHEN
G COOPER
J DESPIRITO
B GUIDOS
K HEAVEY
X HUANG
J NEWILL
P PLOSTINS (5 CPS)
J SAHU
S SILTON
D WEBB
P WEINACHT
AMSRD ARL WM BF
R PEARSON
S WILKERSON
AMSRD ARL WM TC
R SUMMERS

INTENTIONALLY LEFT BLANK.